Controllable Preferential-Etching Synthesis and Photocatalytic Activity of Porous ZnO Nanotubes

Hongqiang Wang, Guanghai Li,* Lichao Jia, Guozhong Wang, and Chunjuan Tang

Key Laboratory of Materials Physics, Anhui Key Laboratory of Nanomaterials and Nanotechnology, Institute of Solid State Physics, Chinese Academy of Sciences, Hefei 230031, P. R. China

Received: April 9, 2008; Revised Manuscript Received: May 11, 2008

Porous ZnO nanotubes have been synthesized via a facile hydrothermal method based on a preferential etching strategy. The nanotubes have a nearly homogeneous size with about 250 nm diameter, 40 nm wall thickness, and 500 nm length. Nanoholes with diameters ranging from tens to hundreds of nanometers were created on the side wall of the tubular structure. Formation of the porous ZnO nanotubes resulted from preferential etching along the *c* axis and relatively slow etching along the radial directions due to the polar feature of the ZnO crystal. Superior photocatalytic activity of the porous ZnO nanotubes in the degradation of methyl orange compared to the other samples has been demonstrated, and the origin is mainly ascribed to the scattered nanoholes on the wall of the porous nanotubes. The influence factors and formation mechanism of the porous ZnO nanotubes were analyzed and discussed.

1. Introduction

Metal oxide porous nanostructures have been of great interest in catalysis,[1,2] sensors,[3] filters in separation,[4] and building blocks in tissue engineering,[5] because of their high specific surface area and high porosity. To date, different methods, such as chemical vapor deposition,[6,7] aqueous chemical strategies relying on the use of surfactants,[8,9] and two-dimensional colloidal crystal template techniques,[10,11] have been explored to fabricate the porous nanostructures. Despite these proven successes in growing porous materials, developing simple and low-cost synthetic technologies to fabricate porous nanoarchitectures that could be functional elements of future devices still remains a long-term challenge.

Zinc oxide, with band gap of 3.37 eV and a high exciton bound energy of 60 meV at room temperature, has aroused tremendous research interest in recent years due to its distinguished performance in optics, electronics, and photonics,[12–14] and has been shown the richest range of morphologies such as nanowires, nanobelts, nanorods, and nanodisks among the wide band gap semiconductors.[15–17] Promising performance in gas sensing and photocatalysis has been demonstrated in these nanomaterials.[18–26] Nevertheless, the sensor capability and catalysis efficiency are relatively low because of the inherent low porosity of these nanomaterials. The tubular nanostructure is considered the most promising morphology used in the fields of gas sensors and photocatalysis due to its high porosity and large specific surface area,[27,28] but in practical application, these advantages could not be fully embodied due to the fact that the reaction gas or pollutants cannot diffuse into the innermost part of the nanotube. Therefore, exploring the fabrication of nanotube-based sensors/catalysts whose active surfaces are extended to the inner surfaces is essential for the development of advanced gas sensors and catalysts.[29]

In general, the polar crystal of ZnO nanostructures grow preferentially along [0001] direction (+*c* axis terminated by zinc) because of the lowest surface energy of the (0002) facet, and the growth velocity along other directions is relatively low.[30] Recently, it has been reported that the etching direction of the ZnO nanostructure is also preferential, in which the etching rate along the *c* axis is faster than that in the radial direction, and thus the tubular nanostructure could be formed easily.[31] This result inspires us to evaluate whether such an etching rate difference can be used to synthesize a tubular nanostructure with nanoholes on its side walls for easy gas/dye molecule diffusion into the nanotubes.

In this paper, we report the low-temperature synthesis of ZnO nanotubes with nanoscaled holes on the side walls via a two-step hydrothermal method based on the preferential etching strategy, and superior photocatalytic activity of the porous ZnO nanotubes in the degradation of methyl orange compared to the other samples has been demonstrated.

2. Experimental Section

2.1. Synthesis. All reagents, including zinc chloride ($ZnCl_2$) and ammonia ($NH_3 \cdot H_2O$) were analytical grade and used without further purification. In a typical procedure, 80 mL of 0.1 M $ZnCl_2$ solution was first prepared, and then 4 mL ammonia (25%) was dropped slowly (about 0.6−0.8 mL/min) into the solution under magnetic stirring. The solution was stirred for 10 min, and then transferred into a Teflon autoclave. A silicon wafer suspended horizontally about 5 mm below the solution surface was used to collect the products. The autoclave was put in an oven first at 95 °C for 70 min (the first heat treatment), and then the oven was cooled rapidly at a rate of about 40 °C/min to 75 °C and maintained at this temperature for 120 min (the second heat treatment), and finally the autoclave was cooled down naturally to room temperature. The substrate was rinsed with deionized water several times to remove any residual salts or amine complexes in the final product and dried naturally before further characterization.

2.2. Characterization. The morphology of the products was examined by field emission scanning electron microscopy (FESEM, Sirion 200), transmission electron microscope (TEM, JEM-2010), and high-resolution transmission electron microscope (HRTEM, JEOL 2010). The crystal structure was characterized by X-ray diffraction (XRD) using Cu $K\alpha_1$ line (Philips X'Pert).

* Corresponding author. Email: ghli@issp.ac.cn.

10.1021/jp803059k CCC: $40.75
Published on Web 07/16/2008

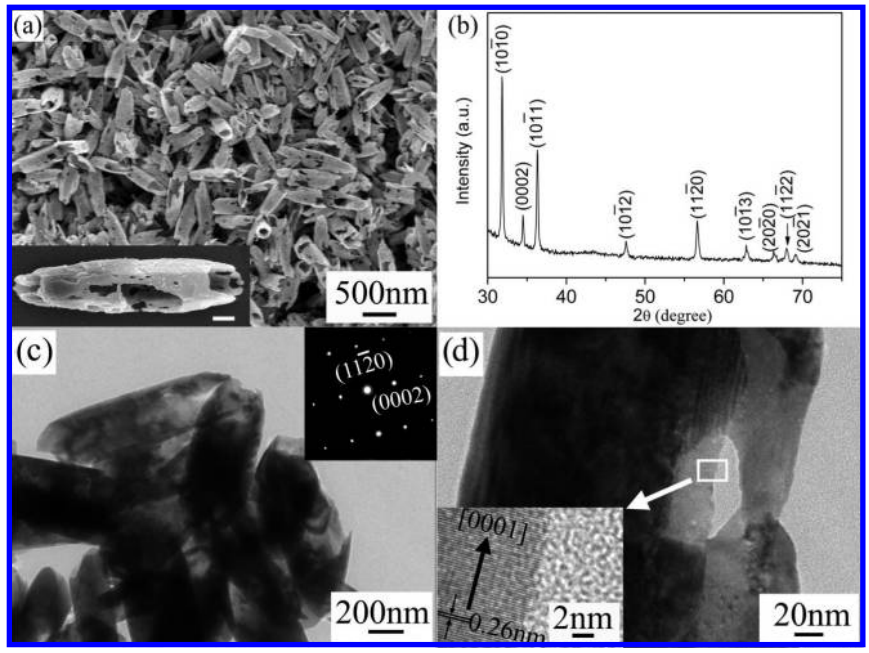

Figure 1. (a) FESEM image of the porous ZnO nanotubes; the inset is the FESEM image of a single porous ZnO nanotube (scale bar 200 nm). (b) XRD pattern of the porous ZnO nanotubes. (c) TEM image of the porous ZnO nanotubes; the inset is the corresponding selected area diffraction pattern. (d) TEM image of a typical nanohole on the side wall of a porous ZnO nanotube; the inset is the HRTEM image of the square area.

2.3. Photocatalytic Activity Measurement. The reaction suspension was prepared by adding 15 mg porous ZnO nanotube (scraped from the Si substrate) into 80 mL of methyl orange (MO, 10^{-5} M) solution. The suspension was irradiated using the high-pressure Hg lamp (125 W, 8 cm away from the suspension) under continuous stirring at room temperature (an electric fan was used to avoid temperature increase of the reaction solutions during UV light irradiation). Before irradiation, the aqueous solution was magnetically stirred in the dark for 30 min to reach the adsorption equilibrium of MO with the catalyst. Analytical samples for absorption measurement were taken out from the reaction suspension at different time intervals and centrifuged at 12 000 rpm for 10 min to remove the porous ZnO nanotubes. A spectrophotometer (CARY-5E) was used to record the UV−vis absorption spectra of the centrifuged solutions. Further comparative experiments including 15 mg commercial anatase TiO_2 nanoparticles, 15 mg ZnO double-layer microdisks,[32] and 15 mg commercial ZnO nanoparticles were also carried out to investigate the photocatalytic activity of the porous ZnO nanotubes.

The durability of the photocatalytic activity of the porous ZnO nanotubes was also studied by reuse of the catalysts under the UV light irradiation, which was performed at the same ratio of the porous ZnO nanotubes to MO. For the first cycle, a 3 mL mixture solution of MO and catalyst was taken out as test samples after the photocatalysis was performed for 30 min, and another 3 mL mixture solution for 60 min. For the second cycle, the photocatalyst was first recollected after the first cycle, then 74 mL fresh MO aqueous solution was added, and finally the same photocatalysis tests as the first cycle were performed. For the third cycle, 68 mL fresh MO aqueous solution was added, and so on.

3. Results and Discussion

3.1. Characterization of the Porous ZnO Nanotubes. Figure 1a shows typical morphology of the final product. One can see that the products have tubular structures, and the tubes show a nearly homogeneous size of about 250 nm in diameter and 500 nm in length. Careful examination reveals that there are always some scattered nanoholes on the side walls of each nanotube, which makes the nanotube presents a porous feature. The nanoholes with diameters ranging from tens to hundreds of nanometers on the side walls can be clearly seen in the inset in Figure 1a. Figure 1b is the corresponding XRD pattern. As indexed in the pattern, all diffraction peaks match well with the wurtzite ZnO structure with the lattice constants of a = 3.250 Å and c = 5.207 Å. The much weaker intensity of the (0002) peak as compared with that in the standard JCPDS card (36−1451) provides further evidence of the tubular structure, as proposed in the literature.[26,27]

Figure 1c shows a typical TEM image of the porous ZnO nanotubes, which demonstrates that the nanotubes have an outer diameter of about 250 nm and wall thickness of about 40 nm, which is in agreement with the SEM observations. The selected-area electron diffraction pattern of an individual nanotube (the inset in Figure 1c) corresponding to the [1$\bar{1}$00] zone axis of wurzite ZnO confirms that the ZnO nanotube is single crystalline. Figure 1d shows a typical TEM image of a nanotube wall; a nanohole (the bright area) with the size of about 40 nm in width and 60 nm in length can be clearly seen, which further confirms the porous feature of the nanotubes. The clear lattice fringe of the HRTEM image shown in the inset of Figure 1d taken from the bright area is considered to come from the edge of a nanohole because of the coexistence of the lattice fringe and the amorphous carbon film, which indicates that there is another nanohole on the other side wall of the nanotube, and the two nanoholes forms a channel for the two sides of the nanotube. From the lattice fringe, one can see that the crystal planes are perpendicular to the growth direction of the nanotube, and the measured interplane spacing (0.26 nm) matches well with the literature reported value of (0002) plane in wurtzite ZnO (lattice parameter = 0.26 nm), which provides further evidence that the nanotubes grow along the [0001] direction.

3.2. Preferential-Etching Induced Growth of the Porous ZnO Nanotubes. TEM analyses show that the tubular structure is single crystalline from the top to the bottom, and the formation of the nanohole at the middle of the nanotube seems hard to

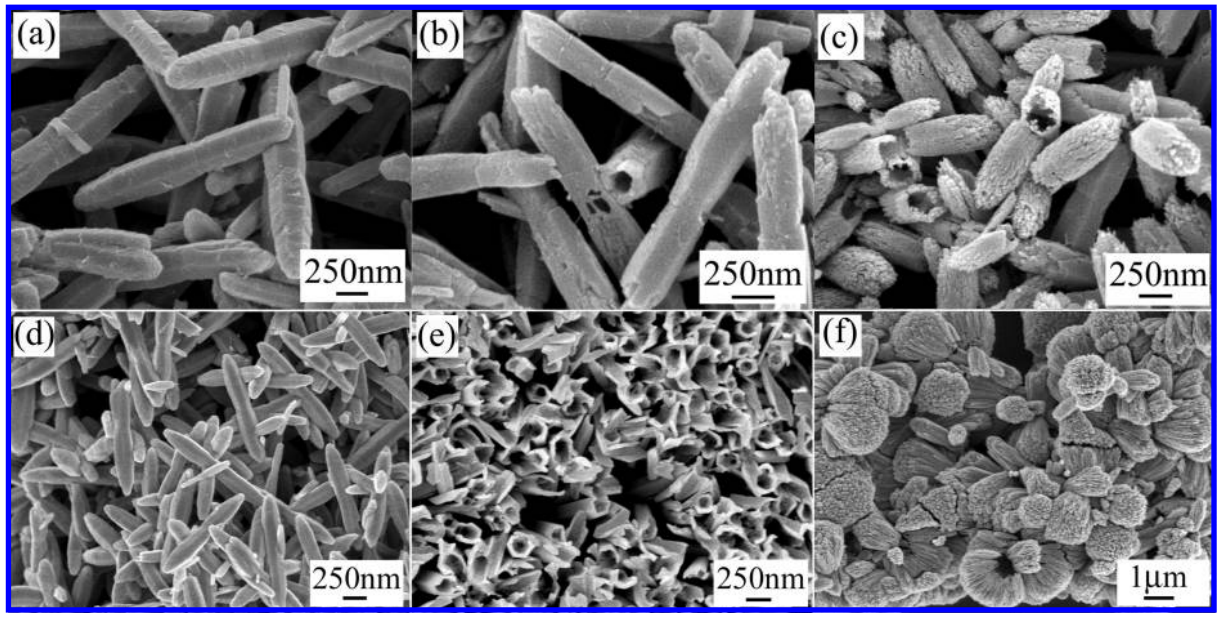

Figure 2. FESEM images of the product after the second heat treatment for times of (a) 30 min, (b) 60 min, and (c) 90 min. FESEM images of the product obtained at the conditions of (d) reaction in an open air condition, (e) at the second reaction temperature of 60 °C, and (f) with a fast ammonia dropping rate.

explain from crystal chemistry or solid-state chemistry. To account for the formation mechanism of the nanhole, experiments with different heating times were performed. The FESEM images of the products obtained at different time periods at the second heat treatment are shown in Figure 2. When heat-treated for 30 min, the product is dominated by nanorods with the size of about 250 nm in diameter and 1−2 μm in length, as shown in Figure 2a, which is similar in morphology to the products obtained at the first heat treatment. Careful examination indicates that each nanorod is a paired rod. For product heating for 60 min, the size of the nanorods remains unchanged and some nanoholes mainly situated at the circled trench area of the nanorods can be observed, as shown in Figure 2b. Figure 2c shows the morphology of the products heated for 90 min; many hollow structures with nearly the same diameter and half-length of the nanorods are formed, and the surface of the hollow structure becomes rougher than that of the nanorod shown in Figure 2a,b. When heating time was increased to 120 min, tubular structures with a nearly homogeneous size of about 250 nm in diameter and 500 nm in length are formed, and there are many nanoholes on the side walls of each nanotube, as illustrated in Figure 1a. It was found that further increasing the heating time would lead to the breaking of the nanotubes (see the Supporting Information). It can be concluded from this result that the appearance of the nanoholes is not at the initial crystal growth stage but after the formation of the single crystal nanorods.

Several experiments were carried out to determine the parameters other than temperature that are important for the formation of porous nanotubes, such as the pressure of the autoclave, the temperature of the second heat treatment, the depth of the silicon wafer located in the precursor solution, and the dropping rate of ammonia in the solution. It was found that only the paired nanorods with size of about 250 nm in diameter and 1−2 μm in length were formed in open air or in a partially sealed autoclave (see Figure 2d). The etching time to form the porous ZnO nanotubes depends on the depth of the Si wafer located inside the solution—the deeper the Si wafer, the longer the etching time—and no porous ZnO nanotubes were found if the Si wafer was put on the bottom of the autoclave. If the temperature of the second heat treatment is lower than 75 °C, such as 60 °C, groove-shaped ZnO nanostructures instead of porous tubular structures were obtained (see Figure 2e). A rapid dripping rate of the ammonia (for example, adding the ammonia within 30 s) will lead to an increase in diameter of the nanorods from nanometer scale to micrometer scale, and the morphology of these microrods remains unchanged even after an ultralong heating at 75 °C (see Figure 2f).

On the basis of the information we have gathered, a growth mechanism of the porous nanotubes can be proposed. From the crystallography, ZnO can be described as a number of alternating planes composed of tetrahedrally coordinated O^{2-} and Zn^{2+} ions, staked alternately along the *c* axis. Generally, the positively Zn^{2+} terminated (0001) and negatively O^{2-} terminated $(000\bar{1})$ polar surfaces have high surface energies, and the growth of the crystal will be preferentially along the *c* axis. In present study, the first growth stage corresponds to the transformation of a large amount of the precursor $Zn(NH_3)_4^{2+}$ into ZnO deposition through hydrothermal decomposition at a higher temperature of 95 °C, leading to the formation of a single crystal ZnO nanorod (Figure 3a). At the same time, ZnO also dissolves according to reaction 1 as the equilibrium moves to the left. However, the growth of ZnO is dominant because the high concentration of $Zn(NH_3)_4^{2+}$ favors precipitation of ZnO at 95 °C. On the other hand, the etching rates of the ZnO crystal along the *c* axis is faster than that in the other directions. As the temperature quickly cools down from 95 °C to 75 °C together with the partial consumption of the $Zn(NH_3)_4^{2+}$ in the solution, reaction 1 will shift to the left, leading to the etching of the ZnO nanorods. The etching of the paired nanorods in the present study begins at the center of the nanorod, which is just the nucleation site, and this might be attributed to the fact that the nucleation site has high activity both for growth and for etching (Figure 3b). Further etching at the center of the paired nanorod leads to its splitting and the atoms in the metastable (0001) planes are removed at the next process owing to the polar feature of the ZnO crystal, leading to the hollowing of the splitted nanorods and the formation of the tubular structures (Figure 3c).

$$Zn(NH_3)_4^{2+} + OH^- \rightleftharpoons ZnO + NH_3 + H_2O \quad (1)$$

Here, it should be noted that, when the chemical etching is preferentially along the *c* axis, the dissolution of ZnO along the radial directions also proceeds at a relatively slow rate. As reported in our previous work, at 75 °C, a nonequilibrium reaction in which simultaneously deposited and dissolution of ZnO is created and long reaction time at 75 °C favors the formation of complex defect species.[33] Due to the heterogeneous distribution of defects/strain on the outer side walls, the etching along the radial direction is heterogeneous, in which the defect sites have higher etching/reaction rates.[34] With the formation of the tubular structure, the atoms on the side walls are removed heterogeneously, leading to the roughness of the side walls and the subsequent formation of the nanoholes with heterogeneous distribution (Figure 3d). The formation of the paired nanorods, as seen in Figure 2a, is considered to be due to the existence of a polar field pointed to the Zn^{2+}-terminated surface from the O^{2-}-terminated surface (see Figure 3e); the growth of the nanorod will counterbalance the polar field,[32] and thus the nanorod will form a symmetrical structure with two parts of nearly the same length. In an alkaline medium, the crystal growth rates of ZnO in different directions obeys the relationship $\{000\bar{1}\} > \{01\bar{1}\bar{1}\} > \{01\bar{1}1\} > \{0001\}$.[35] The plane with the faster growth rate will disappear earlier, and the $\{01\bar{1}\bar{1}\}$ and $\{01\bar{1}1\}$ planes will thus subsequently gradually disappear, leading to the formation of a circled trench in the center of the paired nanorods, making the diameter slightly different from the two ends to the center.

The synthesis of porous ZnO nanotubes is in a controllable manner, which is mainly because the chemical equilibrium state in the present study (shown in reaction 1) is sensitive to the reaction conditions, such as the pressure of the autoclave, the temperature of the second heat treatment, and the depth of the silicon wafer located in the precursor solution. Low pressure in the autoclave and a deeper location of the substrate in the autoclave will result in a lower concentration of NH_3 dissolved in the solution, and thus the equilibrium will move to the left in a slower step, leading to a relatively long time for the formation of the porous nanotubes. If the second heat treatment temperature is lower than 75 °C, such as 60 °C, it will result in a higher reaction rate toward the ZnO dissolution and lead to a higher etching rate, and thus the control of the etching process will become difficult.

3.3. Photoctalytic Performance of the Porous Nanotubes. The as-prepared porous ZnO nanotubes have been tested for the applicability in photodegrading organic dyes of methyl orange. Figure 4a shows the absorption spectra of aqueous solution of MO (1.0×10^{-5} M, 80 mL) in the presence of the porous ZnO nanotubes (15 mg) irradiated by a UV lamp at different periods of time. The absorption peak corresponding to the MO molecules at 464 nm rapidly decreases in intensity with the prolonging of the exposure time, and disappears almost completely after about 60 min. No new absorption peaks appear in the whole spectra.

Further comparative experiments were carried out to investigate the photocatalytic activity of the porous ZnO nanotubes, including (b) 15 mg commercial anatase TiO_2 nanoparticles, (c) 15 mg ZnO double-layer microdisks, and (d) 15 mg commercial ZnO nanoparticles, and corresponding absorption spectra are shown in Figure 4. It could be observed that the absorption peak of the MO molecules still exists after 60 min exposure time for the TiO_2 nanoparticles and ZnO double-layer microdisks, while for the ZnO nanoparticles, the absorption peak nearly disappears after about 50 min of exposure time.

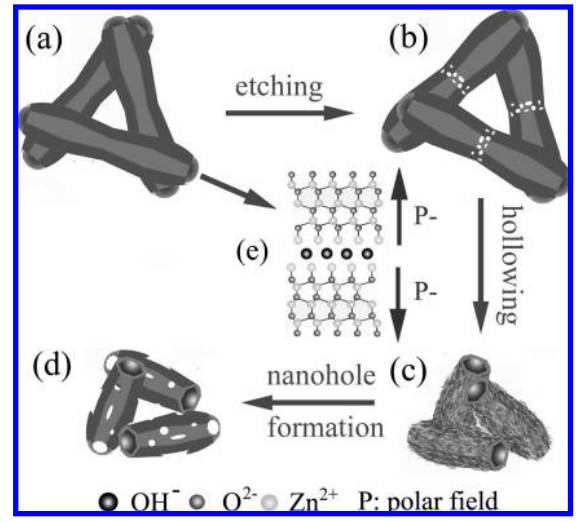

Figure 3. Schematic illustrations of the formation mechanism of the porous ZnO nanotubes: (a) formation of a paired nanorod, (b) etching at the center of the paired nanorods, (c) further etching leading to the splitting and hollowing of the paired nanorods, and (d) radial etching leads to the formation of nanoholes on the side walls. (e) Polar field counterbalance leads to the formation of the paired nanorods.

The comparative results shown in Figure 5 demonstrate that the degradation rate of MO for the porous ZnO nanotubes (curve 1 in Figure 5) is much higher than that for both the ZnO double-layer microdisks (curve 2 in Figure 5) and the TiO_2 nanoparticles (curve 3 in Figure 5), in which 52% MO still exists even after 60 min irradiation for the TiO_2 nanoparticles and 27% for the ZnO double-layer microdisks. Despite the fast degradation rate of the commercial ZnO nanoparticles within the first 20 min (nearly 80% degradation), the degradation rate slows down dramatically in the subsequent 30 min (see curve 4 in Figure 5), and the cause is mainly ascribed to the easy aggregation in the solution and easy adherence to the vessel wall of the ZnO nanoparticles after 20 min of stirring, which is similar to the case for TiO_2 nanoparticles. This phenomenon does not happen for the porous ZnO nanotubes, indicating that the recyclable feature of the porous ZnO nanotubes is superior to both ZnO and TiO_2 nanoparticle.

Although the specific surface area of the double-layer ZnO microdisks (22.9924 m^2/g) is smaller than that of the TiO_2 nanoparticles (41.0680 m^2/g), the degradation rate of MO of the former is faster than that of the latter. The easy aggregation of the nanoparticles could be one of the reasons. On the other hand, the photocatalytic efficiency is surface-dependent to some extent, and the organic dyes could be degraded only if they adsorb on the surface of the catalyst and the high-activity polar planes dominate the photochemical processes in degrading the organic dyes.[36]

To further investigate the concentration change of the MO molecules in the porous ZnO nanotube catalytic measurements, another two experiments were carried out: (i) without any catalyst but with UV light irradiation to determine the natural decrease of the MO concentration; (ii) adsorption experiments were carried out in darkness to examine whether the physisorption/chemisorption of the porous ZnO nanotubes plays an important role in the rapid decrease of the MO concentration. The result is also shown in Figure 5 (see curves 5 and 6, respectively). Very little MO photodegradation can be observed without any catalyst under UV light irradiation (less than 5% within 60 min; curve 5 in Figure 5). The adsorption plays a relatively more important role in the decrease of the MO

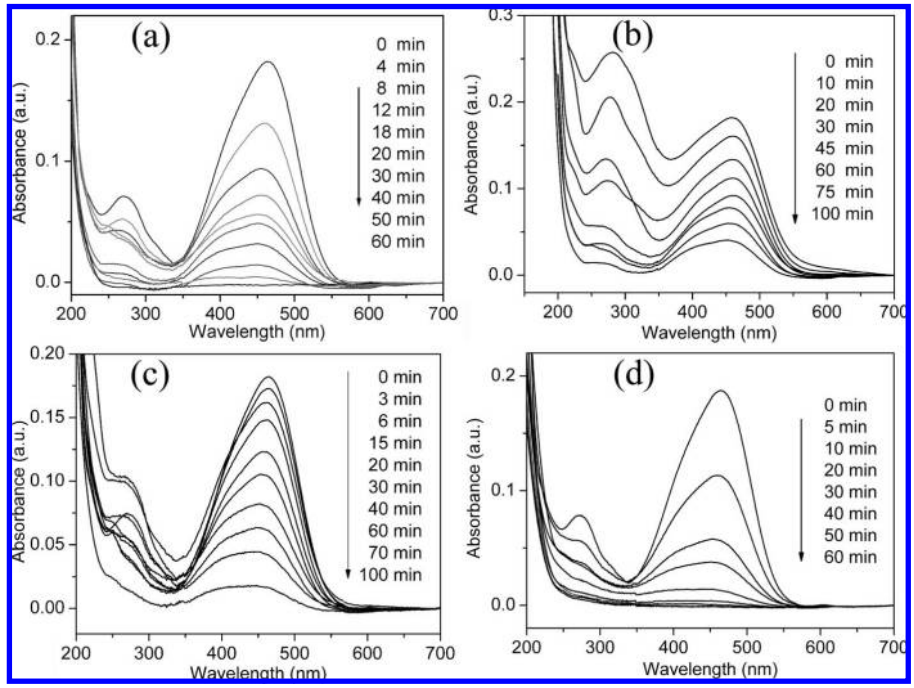

Figure 4. Adsorption spectra of methyl orange solutions in the presence of (a) porous ZnO nanotubes, (b) anatase TiO_2 nanoparticles, (c) ZnO double-layer microdisks, and (d) commercial ZnO nanoparticles irradiated by a UV lamp at different periods of time.

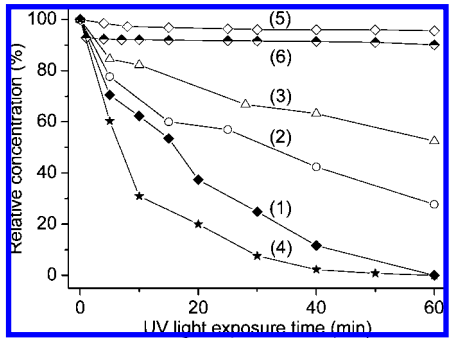

Figure 5. Photodegradation kinetics of methyl orange in the presence of 15 mg of (curve 1) porous ZnO nanotubes, (curve 2) commercial anatase TiO_2 nanoparticles, (curve 3) ZnO double-layer microdisks, (curve 4) commercial ZnO nanoparticles, (curve 5) no catalyst, and (curve 6) 15 mg of porous ZnO nanotubes without UV light irradiation.

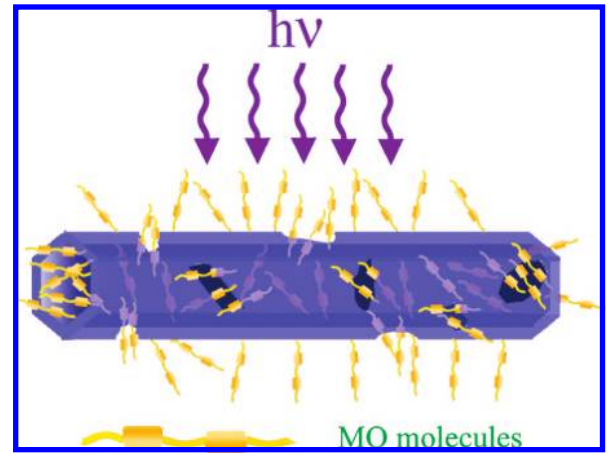

Figure 6. Schematic illustration of the accelerated diffusion of dye molecules into the inner part of the nanotube leading to high photocatalytic activity.

concentration, and after 60 min stirring in darkness, nearly 10% decrease of the MO concentration can be detected, as shown in curve 6 in Figure 5. It should be noted that it took only about 1 min to reach the maximum adsorption on the porous ZnO nanotubes with about 8% decrease of the MO concentration. This fast adsorption and nearly 8% decrease of the MO concentration are considered related to the peculiar porous nanostructure. Nevertheless, when the MO reaches 100% degradation, the room-temperature photodegradation of the porous ZnO nanotubes dominates the decrease of the MO concentration (about 85%).

The origin of the higher photocatalytic activity of the porous ZnO nanotubes is mainly ascribed to the high specific surface area contributed by both the active outer and inner surfaces of the nanotubes. However, this point alone cannot fully interpret the fast degradation. For the porous ZnO nanotubes in the present study, there are two unique advantages in the photocatalysis which might be helpful to understand the fast photocatalysis performance: (i) the nanoholes on the side walls provide ideal channels for easy and fast diffusion of the dye molecules into the inner tube part, which greatly increases the chances and velocities of the encounter of the produced electron−hole pair with the dye molecules and thus enhances the photocatalytic activity; (ii) because the nanoholes are heterogeneously distributed on the side walls, the porous nanotubes are transparent for the UV light, which greatly increases the utilizing efficiency of the UV light, as shown in Figure 6.

The durability of the photocatalytic activity of the porous ZnO nanotubes was also studied by reuse of the catalysts under UV light irradiation. Figure 7 shows the photodegradation results for five cycles using the porous ZnO nanotubes. For each cycle, we took 3 mL of the MO solution in which catalysis had been performed for 30 and 60 min. One can see that the degradation rate decreased slowly, and there is still some MO after 60 min of irradiation after the first cycle (see Figure 7a). The slowdown of the degradation rate can be clearly observed via the overall degradation of MO after 60 min of irradiation, as shown in Figure 7b. Even after 5 cycles, the degradation rate of porous ZnO nanotubes still remains above 92.5%, indicating relatively

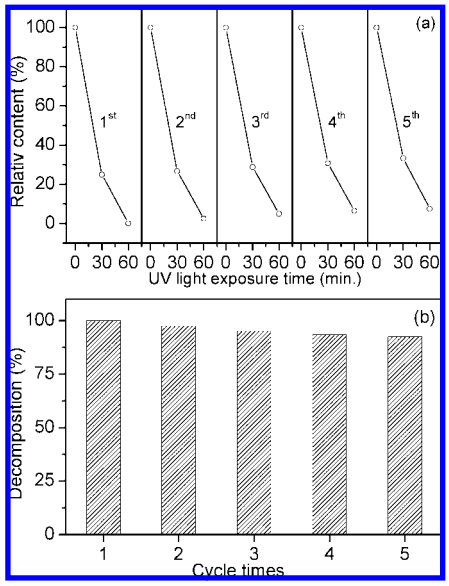

Figure 7. (a) Photodegradation performance of porous ZnO nanotubes toward 10^{-5} M MO solutions within five cycles and (b) durability of the porous ZnO nanotubes under UV light for the five cycles.

high durability of the photodegradation of the porous ZnO nanotubes. The slowdown of the degradation rate of ZnO catalyst after several cycles was also observed in the literature;[37] however, the detailed mechanism is not clear yet.

4. Conclusions

In summary, we have demonstrated a facile hydrothermal method to synthesize porous ZnO nanotubes with scattered nanoholes on the side walls. The nanotubes have an average diameter of about 250 nm and length of about 500 nm, and the nanoholes have sizes ranging from tens to hundreds of nanometers. It was found that the pressure of the autoclave, the temperature and reaction time of the second heat treatment, and the dropping rate of ammonia play important roles in the formation of the porous nanotubes. The formation mechanism of the porous ZnO nanotube is mainly due to the preferential etching along the polar axis and slow etching along the radial directions. Superior photocatalytic activity of the porous ZnO nanotube in the degradation of methyl orange compared to the commercial ZnO powders, ZnO double-layer microdisks, and anatase TiO_2 nanoparticles has been demonstrated. The scattered nanoholes not only make the inner surface applicable to the degradation, but also facilitate easier and faster diffusion of the dye molecules into the inner part of the nanotube, which greatly increases the efficiency of the UV light. The porous ZnO nanotubes are expected to find potential applications in environmental remediation and toxic gas treatment. Furthermore, the synthesis strategy of the porous nanotube may be helpful to fabricate other metal oxide nanotubes with active inner surfaces.

Acknowledgment. This work was financially supported by the National Natural Science Foundation of China (Grant No. 10674137) and National Basic Research Program of China (Grant No. 2007CB936601).

Supporting Information Available: FESEM images of the product after the second heat treatment for 150 and 180 min. FESEM images of the anatase TiO_2 nanoparticles, ZnO double-layer microdisks, and commercial ZnO powders. Adsorption spectra of methyl orange solutions in the presence of UV lamp without any catalyst, and adsorption spectra of methyl orange solutions using 15 mg of porous ZnO nanotubes in darkness at different periods of time. This material is available free of charge via the Internet at http://pubs.acs.org.

References and Notes

(1) Zapilko, C.; Liang, Y.; Nerdal, W.; Anwander, R. *Chem. Eur. J.* **2007**, *13*, 3169.
(2) Vasylyev, M. V.; Wachtel, E. J.; Popovitz-Biro, R.; Neumann, R. *Chem. Eur. J.* **2006**, *12*, 3507.
(3) Sun, F. Q.; Cai, W. P.; Li, Y.; Jia, L. C.; Lu, F. *Adv. Mater.* **2005**, *17*, 2872.
(4) Kresge, C. T.; Leonowicz, M. E.; Roth, W. J.; Vartuli, J. C.; Beck, J. S. *Nature* **1992**, *359*, 710.
(5) Hubbell, J. A.; Langer, R. *Chem. Eng. News* **1995, March 13**, 42.
(6) Wang, X. D.; Summers, C. J.; Wang, Z. L. *Adv. Mater.* **2004**, *16*, 1215.
(7) Wang, X. D.; Gao, P. X.; Li, J.; Summers, C. J.; Wang, Z. L. *Adv. Mater.* **2002**, *14*, 1732.
(8) Hu, J. -S.; Ren, L. -L.; Guo, Y. -G.; Liang, H. -P.; Cao, A. -M.; Wan, L. -J.; Bai, C.-L. *Angew. Chem., Int. Ed.* **2005**, *44*, 1269.
(9) Wang, X. C.; Yu, J. C.; Yip, H. Y.; Wu, L.; Wong, P. K.; Lai, S. Y. *Chem. Eur. J.* **2005**, *11*, 2997.
(10) Li, Y.; Cai, W. P.; Cao, B. Q.; Duan, G. T.; Li, C. C.; Sun, F. Q.; Zeng, H. B. *J. Mater. Chem.* **2006**, *16*, 609.
(11) Sun, F. Q.; Cai, W. P.; Li, Y.; Cao, B. Q.; Lei, Y.; Zhang, L. D. *Adv. Funct. Mater.* **2004**, *14*, 283.
(12) Hsu, C.-L.; Chang, S.-J.; Lin, Y.-R.; Tsai, S.-Y.; Chen, I.-C. *Chem. Commun.* **2005**, 3571.
(13) Cao, B. Q.; Teng, X. M.; Heo, S. H.; Li, Y.; Cho, S. O.; Li, G. H.; Cai, W. P. *J. Phys. Chem. C* **2007**, *111*, 2470.
(14) Wang, Z. L. *Appl. Phys. A: Mater. Sci. Process.* **2007**, *88*, 7.
(15) Lu, C. H.; Qi, L. M.; Yang, J. H.; Tang, L.; Zhang, D. Y.; Ma, J. M. *Chem. Commun.* **2006**, 3551.
(16) Wu, X. F.; Bai, H.; Li, C.; Lu, G. W.; Shi, G. Q. *Chem. Commun.* **2006**, 1655.
(17) Liu, Y.; Dong, J.; Hesketh, P. J.; Liu, M. *J. Mater. Chem.* **2005**, *15*, 2316.
(18) Liao, L.; Lu, H. B.; Li, J. C.; He, H.; Wang, D. F.; Fu, D. J.; Liu, C. *J. Phys. Chem. C* **2007**, *111*, 1900.
(19) Kuo, T. J.; Lin, C. N.; Kuo, C. L.; Huang, M. H. *Chem. Mater.* **2007**, *19*, 5143.
(20) Ye, C. H.; Bando, Y.; Shen, G.; Golberg, Z. D. *J. Phys. Chem. B* **2006**, *110*, 15146.
(21) Liao, L.; Lu, H. B.; Li, J. C.; Liu, C.; Fu, D. J.; Liu, Y. L. *Appl. Phys. Lett.* **2007**, *91*, 173110.
(22) Zhao, F.; Li, X.; Zheng, J. G.; Yang, X.; Zhao, F.; Wong, K. S.; Wang, J.; Lin, W.; Wu, M.; Su, Q. *Chem. Mater.* **2008**, *20*, 1197.
(23) Sun, T.; Qiu, J.; Liang, C. *J. Phys. Chem. C* **2008**, *112*, 715.
(24) Cho, P.-S.; Kim, K.-W.; Lee, J.-H. *J. Electroceram.* **2006**, *17*, 975.
(25) Wang, H. T.; Kang, B. S.; Ren, F.; Tien, L. C.; Sadik, P. W.; Norton, D. P.; Pearton, S. J.; Lin, J. S. *Appl. Phys. Lett.* **2005**, *86*, 243503.
(26) Wang, J. X.; Sun, X. W.; Yang, Y.; Huang, H.; Lee, Y. C.; Tan, O. K.; Vayssieres, L. *Nanotechnology* **2006**, *17*, 4995.
(27) Wang, J. X.; Sun, X. W.; Huang, H.; Lee, Y. C.; Tan, O. K.; Yu, M. B.; Lo, G. Q.; Kwong, D. L. *Appl. Phys. A: Mater. Sci. Process.* **2007**, *88*, 611.
(28) Lu, H. B.; Li, H.; Liao, L.; Tian, Y.; Shuai, M.; Li, J. C.; Hu, M. F.; Fu, Q.; Zhu, B. P. *Nanotechnology* **2008**, *19*, 045605.
(29) Jung, H. Y.; Jung, S. M.; Kim, J. R.; Suh, J. S. *Appl. Phys. Lett.* **2007**, *90*, 153114.
(30) Wang, Z. L. *J. Phys.: Condens. Matter* **2004**, *16*, R829.
(31) Vayssieres, L.; Keis, K.; Hagfeldt, A.; Lindquist, S.-E. *Chem. Mater.* **2001**, *13*, 4395.
(32) Jia, L. C.; Cai, W. P.; Wang, H. Q.; Zeng, H. B. *Cryst. Growth Des.*, 2007, submitted.
(33) Wang, H. Q.; Wang, G. Z.; Jia, L. C.; Tang, C. J.; Li, G. H. *J. Phys. D: Appl. Phys.* **2007**, *40*, 6549.
(34) Li, F.; Ding, Y.; Gao, P. X.; Xin, X. Q.; Wang, Z. L. *Angew. Chem., Int. Ed.* **2004**, *43*, 5238.
(35) Li, W. J.; Shi, E. W.; Zhong, W. Z.; Yin, Z. W. *J. Cryst. Growth* **1999**, *203*, 186.
(36) Jang, E. S.; Won, J.-H.; Hwang, S.-J.; Choy, J.-H. *Adv. Mater.* **2006**, *18*, 3309.
(37) Lu, F.; Cai, W. P.; Zhang, Y. G. *Adv. Func. Mater.* **2008**, *18*, 1047.

JP803059K